Available online at www.sciencedirect.com
SCIENCE DIRECT®
International Journal of Heat and Mass Transfer 49 (2006) 2097–2112
International Journal of HEAT and MASS TRANSFER
www.elsevier.com/locate/ijhmt

Numerical study on the dopant concentration and refractive index profile evolution in an optical fiber manufacturing process

Y. Yan, R. Pitchumani *

Advanced Materials and Technologies Laboratory, Department of Mechanical Engineering, University of Connecticut, 191 Auditorium Road, Unit 3139, Storrs, CT 06269-3139, USA

Received 2 October 2005; received in revised form 23 November 2005
Available online 23 March 2006

Abstract

The index of refraction is an important property of optical fibers, since it directly affects the bandwidth and optical loss during information transmission. The refractive index is governed by the dopant concentration distribution across the fiber cross section, which is strongly influenced by the processing conditions. An understanding of the effects of process parameters on the dopant concentration profile evolution is important to design the drawing process for tailored refractive index and optical transmission characteristics. Although the heat and momentum transport in optical fiber drawing have been studied extensively, little has been reported in the open literature on dopant concentration and index of refraction profile development during processing. This paper presents a two-dimensional numerical analysis on the flow, heat and mass transfer phenomena involved in the drawing and cooling process of glass optical fibers using a finite difference approach based on primitive variables. The effects of several important parameters are investigated in terms of nondimensional groups, including: fiber draw speed, inert gas velocity, furnace dimensions, gas properties, and dopant properties on the flow, temperature and dopant concentration distribution.

Keywords: Optical fiber; Fiber drawing; Fiber cooling; Refractive index; Dopant diffusion

1. Introduction

Optical fibers, both multimode and single mode, are critical media for transmitting light signals used as information carriers in the communications industry. For multimode fibers, the two basic parameters governing the transmission behavior of the waveguides are fiber core diameter and core refractive index profile. The refractive index profile must be carefully controlled in order to achieve its optimal information carrying capacity [1]. For single mode fibers, cladding diameter is also an important parameter, and a minimum value must be maintained to avoid excessive losses [2]. The refractive index of optical fiber is modified by doping pure silica (SiO_2) with materials such as oxides of germanium, phosphorous and boron. Germanium (Ge) and phosphorous (P) increase the refractive index of SiO_2, while boron (B) decreases it. Since a fiber can guide light only if the refractive index of the core is higher than that of the surrounding region, most fibers consist of a cladding region of pure SiO_2 and a core doped with GeO_2 or P_2O_5 to increase its refractive index, while in some fibers the core is pure SiO_2 and the cladding is doped with B_2O_3 to decrease its refractive index.

The manufacturing process for optical fibers involves preform fabrication, optical fiber drawing, cooling and coating. The preform is preferentially made by the so-called modified chemical vapor deposition process, which includes the deposition of dopants within a fused quartz glass tube by oxidation of gaseous halides at temperatures of 1700–2100 K and subsequent collapsing of the tube into a rod [3]. The preform is then heated to above its melting temperature, while an axial tension is simultaneously

* Corresponding author. Tel.: +1 860 486 0683; fax: +1 860 486 5088.
E-mail address: r.pitchumani@uconn.edu (R. Pitchumani).

0017-9310/$ - see front matter © 2006 Elsevier Ltd. All rights reserved.
doi:10.1016/j.ijheatmasstransfer.2005.11.030

Nomenclature

c	dopant concentration expressed as a mass fraction
c_p	specific heat (J/kg K)
D	diffusion coefficient (m^2/s)
h	heat transfer coefficient for natural convective cooling (W/m^2 K)
k	thermal conductivity (W/m K)
k_B	Boltzmann constant (1.3807×10^{23} J/K)
l	length of the drawing and cooling regions (m)
n	refractive index
p	pressure (N/m^2)
Pe	Peclet number for dopant diffusion
Pr	Prandtl number
r	radial coordinate, radius (m)
Re	Reynolds number
T	physical temperature in absolute scale (K)
u	axial velocity component (m/s)
v	radial velocity component (m/s)
z	axial coordinate (m)

Greek symbols

β	dimensionless axial coordinate in drawing and cooling region
η	dimensionless radial coordinate
μ	dynamic viscosity (N s/m^2)
v	kinematic viscosity (m^2/s)
ρ	density (kg/m^3)
θ	dimensionless temperature

Subscripts

a	inert gas
c	cooling gas
dr	drawing region
f	fiber
F	furnace
fc	forced convection cooling region
m	melting point of fiber
nc	natural convection cooling region
w	wall temperature of the cooling channel

applied to draw the preform into a fiber, a process called drawing. The heating is usually accomplished by feeding the preform into a concentric, cylindrical electric furnace where radiation is the dominant mode of heat transfer [4]. It is during this process that the preform/fiber encounters a drastic change in diameter, temperature, and dopant concentration distribution. Upon exiting the furnace, the fiber undergoes a cooling process, where its temperature is lowered from around its melting temperature of approximately 1900 K to below 500 K [5] through convection and radiation. If the drawing speed of the fiber is very high, forced convective cooling is necessary since natural convection alone will be insufficient to reduce the fiber temperature to the level required by the subsequent coating process. In the coating process, a jacket of polymer material is added to encase the fiber and protect it from scratches that would weaken the fiber's strength. Since the diffusivity of the dopant is very small at low temperatures, the dopant distribution is essentially stabilized at the end of the cooling section and remains unchanged in the coating process. Therefore, the main focus of this study is on the transport phenomena in the optical fiber drawing and cooling regions of the manufacturing process.

In the last three decades, there have been several studies on the temperature profile evolution during the drawing and cooling steps [4–21]. Paek [17] numerically simulated the drawing and cooling process of optical fibers assuming a lumped temperature distribution along the radius, a prescribed temperature for the fiber at the furnace exit, and a prescribed heat transfer coefficient between the fiber and its environment. Jaluria and coworkers [5–9,15,20] have carried out more rigorous studies on the neck-down region by solving the coupled convection, conduction and radiation transport between the furnace muffle and the necked preform. Their results provide detailed information on the heat transfer mechanism in fiber drawing, but in these studies the momentum equations were solved using the stream function–vorticity approach, which is limited to two-dimensional analysis.

Glicksman [11] performed analytical and experimental studies on the cooling process of optical fibers. In his model, a lumped capacity method was used to predict the transient temperature variation in the fiber, while the Nusselt number for the natural convective cooling process was simulated using the Reynolds analogy. Choudhury et al. [5] carried out numerical simulation on the forced cooling of optical fibers prescribing a uniform initial temperature distribution at the entrance of the cooling section. The complete two-dimensional momentum and energy equations for the fiber as well as the cooling gas were solved using a finite difference method based on stream function–vorticity approach. Gossiaux et al. [12] studied forced cooling of optical fibers using a nitrogen–helium mixture as the cooling gas. The effects of the cooling tube diameter and cooling gas property on the cooling rate were studied.

Scarce information is available in the open literature on the theoretical, computational, or experimental study of dopant diffusion during the optical fiber manufacturing process and, consequently, the refractive index prediction. Palmer [22] analytically studied the evolution of temperature and dopant distribution in the cooling of optical fibers assuming a heat transfer coefficient between the fiber and the forced cooling gas.

These studies have provided much information on the heat transfer phenomena during the fiber manufacturing process, but the models have generally ignored the com-

bined effects of the drawing and cooling processes, instead relying on an assumed temperature variation at the junction of the drawing and cooling sections. In order to provide a more realistic solution to the temperature evolution in preform and fiber, this research investigates the conjugate heat transfer problem during the drawing and cooling processes. This study also seeks to address the need for rigorous investigation of dopant diffusion during the manufacturing process of optical fibers, which is presently lacking in the literature.

The objective of this study is to develop a mathematical model for the prediction of the temperature and dopant concentration evolution during the drawing and cooling processes, and the refractive index profile in the fiber. To this end, the model describes the convection, conduction, radiation and species transport during the combined drawing and cooling process. Allied with this objective is the development of a computational framework, which solves the mathematical model formulated in terms of primitive variables, using a control volume based finite difference scheme. Parametric studies are presented to illustrate the effects of the various dimensionless parameters on the temperature and dopant concentration evolution, and the refractive index profile in the paper. Section 2 describes the formulation of the governing equations and the numerical solution procedure. The results of the study are presented and discussed in Section 3.

2. Analysis

Fig. 1 shows a schematic of the drawing and cooling sections considered for the modeling. In the drawing process, laminar axisymmetric flows of the glass preform/fiber and inert gas in a cylindrical furnace are studied. For simplicity, it is assumed that the flow and temperature fields are not significantly affected by the dopant, which is taken as GeO_2 in this study.

Considering the process to be at steady state, the governing equations for mass, momentum, energy and dopant transport can be expressed as

Continuity equation:

$$\frac{\partial(\rho u)}{\partial z}+\frac{1}{r}\frac{\partial(\rho r v)}{\partial r}=0 \tag{1}$$

Momentum equations:

$$\frac{\partial(\rho u^2)}{\partial z}+\frac{1}{r}\frac{\partial(\rho r u v)}{\partial r} =-\frac{\partial p}{\partial z}+2\frac{\partial}{\partial z}\left(\mu\frac{\partial u}{\partial z}\right)+\frac{1}{r}\frac{\partial}{\partial r}\left[r\mu\left(\frac{\partial u}{\partial r}+\frac{\partial v}{\partial z}\right)\right] \tag{2}$$

$$\frac{\partial(\rho u v)}{\partial z}+\frac{1}{r}\frac{\partial(\rho r v^2)}{\partial r} =-\frac{\partial p}{\partial r}+\frac{\partial}{\partial z}\left[\mu\left(\frac{\partial u}{\partial r}+\frac{\partial v}{\partial z}\right)\right]+\frac{2}{r}\frac{\partial}{\partial r}\left(r\mu\frac{\partial v}{\partial r}\right)-\frac{2\mu\cdot v}{r^2} \tag{3}$$

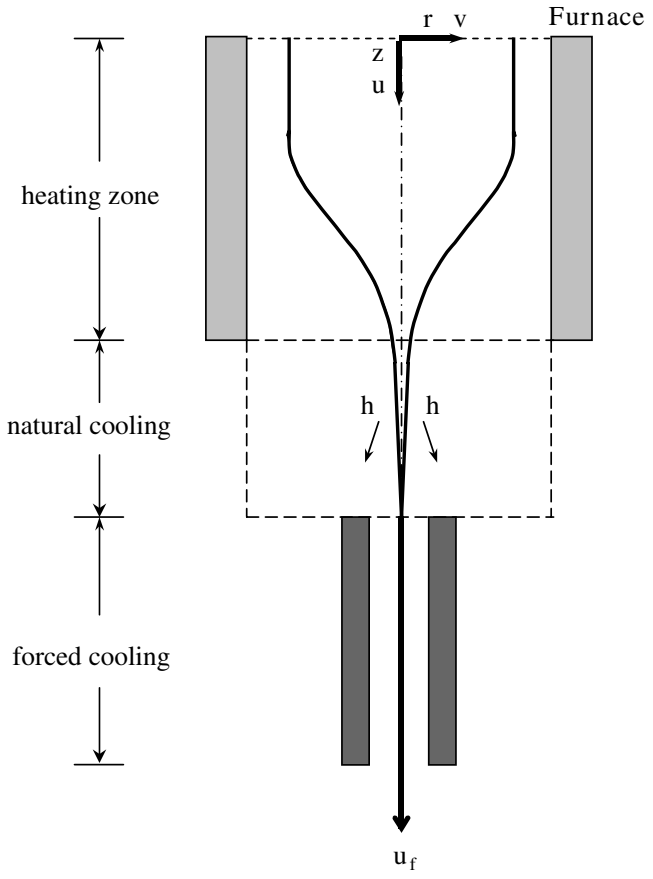

Fig. 1. Schematic of an optical fiber drawing process along the furnace and the cooling zone.

Energy equation:

$$\frac{\partial(\rho c_p u T)}{\partial z}+\frac{1}{r}\frac{\partial(\rho c_p r v T)}{\partial r} =\frac{\partial}{\partial z}\left(k\frac{\partial T}{\partial z}\right)+\frac{1}{r}\frac{\partial}{\partial r}\left(rk\frac{\partial T}{\partial r}\right) +\mu\left\{2\left[\left(\frac{\partial u}{\partial r}\right)^2+\left(\frac{u}{r}\right)^2+\left(\frac{\partial v}{\partial z}\right)^2\right]+\left(\frac{\partial u}{\partial z}+\frac{\partial v}{\partial r}\right)^2\right\} \tag{4}$$

Dopant diffusion equation:

$$\frac{\partial(uc)}{\partial z}+\frac{1}{r}\frac{\partial(rvc)}{\partial r}=\frac{\partial}{\partial z}\left(D\frac{\partial c}{\partial z}\right)+\frac{1}{r}\frac{\partial}{\partial r}\left(rD\frac{\partial c}{\partial r}\right) \tag{5}$$

where all the terms are defined in the nomenclature. The above equations are applicable for the entire drawing and cooling sections, with the exception of the energy equation (Eq. (4)), in which viscous dissipation is negligible in the inert gas in the furnace and cooling sections.

2.1. Drawing region

In the furnace, the diameter of the preform changes drastically in the axial direction. The glass preform has a streamwise variation in radius $r(z)$ as it undergoes necking

into a fiber. This profile depends on the forces acting at the surface and should be obtained as a part of the solution. However, in the interest of reducing the computational intensity of the simulations, a known necking shape reported in the literature is assumed. Both natural convective cooling and forced convective cooling are studied; for natural convective cooling, a known convective coefficient is assumed here using experimental results cited in existing literature, whereas for forced convective cooling, the complete governing equations are solved for fiber and cooling gas. In this study, the neck-down profile is chosen to be consistent with available data from the literature. The lengths of the furnace and the preform are both taken to be 0.3 m, the necking occurs between the distance of 0.04 m and 0.22 m. The necking shape of the preform/fiber is described as the logarithmic function of an eighth-order polynomial [15].

$$\begin{aligned}
&\text{For } z \leqslant 0.04\,\text{m}: \ r(z) = 0.006288\,\text{m}\\
&\text{For } z \geqslant 0.22\text{m}: \ r(z) = 0.000059\,\text{m}\\
&\text{For } 0.04\,\text{m} \leqslant z \leqslant 0.22\,\text{m}:\\
&\log_{10} r(z) = -6.66531\times10^{6}(z-0.02)^{8} + 1.5152\times10^{7}(z-0.02)^{7}\\
&\quad - 6.20906\times10^{6}(z-0.02)^{6} + 1.56512\times10^{5}(z-0.02)^{5}\\
&\quad + 3.0826\times10^{5}(z-0.02)^{4} - 4.71803\times10^{4}(z-0.02)^{3}\\
&\quad + 7.884\times10^{2}(z-0.02)^{2} + 15.7224(z-0.02)\\
&\quad - 22.31642
\end{aligned} \tag{6}$$

The complex physical domain is transformed into a right cylindrical domain amenable to a computational implementation using the Laudau's transformation applied to the preform/fiber and inert gas within the furnace.

For preform/fiber:

$$\beta = \frac{z}{l_{\mathrm{dr}}} \quad \text{and} \quad \eta = \frac{r}{r(z)} \tag{7}$$

For inert gas:

$$\beta = \frac{z}{l_{\mathrm{dr}}} \quad \text{and} \quad \eta = \frac{r_{\mathrm{F}} - r}{r_{\mathrm{a}}} = f(k_r, r_{\mathrm{a}}) \tag{8}$$

where

$$k_r = r_{\mathrm{F}}/r_{\mathrm{a}} \quad \text{and} \quad r_{\mathrm{a}} = r_{\mathrm{F}} - r(z)$$

One side effect of the coordinate transformation as described in the above paragraphs is that the mass, momentum and energy conservation are not preserved when control volume based finite difference method is applied to solve the generated governing equations, since the velocity field is not orthogonal to the computational domain. This problem can be resolved by the use of curvilinear velocities, which preserves mass, momentum, and energy conservation in the total flow field [23–26]. Therefore, the following velocity transformations are employed:

For preform/fiber:

$$\bar{u} = u \quad \text{and} \quad \bar{v} = -\eta\frac{dr(z)}{dz}u + v \tag{9}$$

For inert gas:

$$\bar{u} = u \quad \text{and} \quad \bar{v} = \eta\frac{dr(z)}{dz}u - v \tag{10}$$

In order to describe the flow, energy, and mass transport in a more generic way, the governing equations are also nondimensionalized by using the following nondimensional groups:

For preform/fiber:

$$U = \frac{\bar{u}}{u_{\mathrm{f}}}, \quad V = \frac{\bar{v}}{u_{\mathrm{f}}}, \quad P = \frac{p}{\rho_{\mathrm{f,m}}u_{\mathrm{f}}^2}, \quad \theta = \frac{T}{T_{\mathrm{m}}}, \quad C = \frac{c}{c_0} \tag{11}$$

$$Re_{\mathrm{f}} = \frac{u_{\mathrm{f}}r_{\mathrm{f}}}{\nu_{\mathrm{f,m}}}, \quad Pr_{\mathrm{f}} = \frac{\nu_{\mathrm{f,m}}}{\alpha_{\mathrm{f,m}}}, \quad Pe = \frac{u_{\mathrm{f}}r_{\mathrm{f}}}{D_{\mathrm{m}}}, \quad R(z) = \frac{r(z)}{r_{\mathrm{f}}} \tag{12}$$

For inert gas:

$$U = \frac{\bar{u}}{u_{\mathrm{a,0}}}, \quad V = \frac{\bar{v}}{u_{\mathrm{a,0}}}, \quad P = \frac{p}{\rho_{\mathrm{a,m}}u_{\mathrm{a,0}}^2}, \quad \theta = \frac{T}{T_{\mathrm{m}}} \tag{13}$$

$$Re_{\mathrm{a}} = \frac{u_{\mathrm{a,0}}r_{\mathrm{F}}}{\nu_{\mathrm{a,m}}}, \quad Pr_{\mathrm{a}} = \frac{\nu_{\mathrm{a,m}}}{\alpha_{\mathrm{a,m}}}, \quad R_{\mathrm{F}} = \frac{r_{\mathrm{F}}}{r_{\mathrm{f}}} \tag{14}$$

where $u_{\mathrm{a,0}}$ is the inert gas velocity at the entrance of the furnace.

Thermophysical properties are nondimensionalized using those at the reference temperature, the melting temperature of the fiber

$$f_\rho = \frac{\rho}{\rho_{\mathrm{m}}}, \quad f_{C_p} = \frac{C_p}{C_{p,\mathrm{m}}}, \quad f_k = \frac{k}{k_{\mathrm{m}}}, \quad f_\nu = \frac{\nu}{\nu_{\mathrm{m}}}, \quad f_D = \frac{D}{D_{\mathrm{m}}} \tag{15}$$

The nondimensionalized governing equations in the preform/fiber can be expressed as

Continuity equation:

$$\frac{1}{L_{\mathrm{dr}}}\frac{\partial\left[R^2(z)\eta U\right]}{\partial\beta} + \frac{\partial[R(z)\eta V]}{\partial\eta} = 0 \tag{16}$$

Momentum equations:

$$\begin{aligned}
&\frac{1}{L_{\mathrm{dr}}}\frac{\partial\left[R(z)^2\eta U^2\right]}{\partial\beta} + \frac{\partial[R(z)\eta UV]}{\partial\eta}\\
&\quad = -\frac{R(z)^2\eta}{L_{\mathrm{dr}}}\frac{\partial P}{\partial\beta} + \frac{R(z)\eta^2}{L_{\mathrm{dr}}}\frac{\mathrm{d}R(z)}{\mathrm{d}\beta}\frac{\partial P}{\partial\eta}\\
&\qquad + \frac{2R(z)^2\eta}{Re_{\mathrm{f}}L_{\mathrm{dr}}^2}\frac{\partial}{\partial\beta}\left(f_\nu\frac{\partial U}{\partial\beta}\right) + \frac{1}{Re_{\mathrm{f}}}\left\{1 + \frac{2\eta^2}{L_{\mathrm{dr}}^2}\left[\frac{\mathrm{d}R(z)}{\mathrm{d}\beta}\right]^2\right\}\\
&\qquad \times\frac{\partial}{\partial\eta}\left(f_\nu\eta\frac{\partial U}{\partial\eta}\right) - \frac{1}{Re_{\mathrm{f}}L_{\mathrm{dr}}^2}\left[\frac{\mathrm{d}R(z)}{\mathrm{d}\beta}\right]^2\frac{\partial}{\partial\eta}\left(f_\nu\eta^3\frac{\partial U}{\partial\eta}\right)\\
&\qquad - \frac{2R(z)^2\eta^2}{Re_{\mathrm{f}}L_{\mathrm{dr}}^2}\frac{\partial}{\partial\beta}\left[\frac{f_\nu}{R(z)}\frac{\mathrm{d}R(z)}{\mathrm{d}\beta}\frac{\partial U}{\partial\eta}\right]\\
&\qquad - \frac{2R(z)\eta^2}{Re_{\mathrm{f}}L_{\mathrm{dr}}^2}\frac{\mathrm{d}R(z)}{\mathrm{d}\beta}\frac{\partial}{\partial\eta}\left(f_\nu\frac{\partial U}{\partial\beta}\right) + \frac{R(z)}{Re_{\mathrm{f}}L_{\mathrm{dr}}^2}\frac{\mathrm{d}R(z)}{\mathrm{d}\beta}\frac{\partial}{\partial\eta}\left(f_\nu\eta^2\frac{\partial U}{\partial\beta}\right)
\end{aligned}$$

$$+\frac{1}{Re_f L_{dr}^2}\left\{R(z)\frac{d^2R(z)}{d\beta^2}-\left[\frac{dR(z)}{d\beta}\right]^2\right\}\frac{\partial}{\partial\eta}(f_v\eta^2U)$$
$$+\frac{R(z)}{Re_f L_{dr}}\frac{\partial}{\partial\eta}\left(f_v\eta\frac{\partial V}{\partial\beta}\right)-\frac{1}{Re_f L_{dr}}\frac{dR(z)}{d\beta}\frac{\partial}{\partial\eta}\left(f_v\eta^2\frac{\partial V}{\partial\eta}\right) \quad (17)$$

$$\frac{1}{L_{dr}}\frac{\partial\left[R(z)^2\eta UV\right]}{\partial\beta}+\frac{\partial\left[R(z)\eta V^2\right]}{\partial\eta}+\frac{R(z)^2\eta^2}{L_{dr}^2}\frac{\partial}{\partial\beta}\left[\frac{dR(z)}{d\beta}U^2\right]$$
$$+\frac{2R(z)\eta^2}{L_{dr}^2}\left[\frac{dR(z)}{d\beta}\right]^2U^2+\frac{R(z)\eta^2}{L_{dr}}\frac{dR(z)}{d\beta}\frac{\partial}{\partial\eta}(UV)$$
$$+\frac{2R(z)\eta}{L_{dr}}\frac{dR(z)}{d\beta}UV$$
$$=-R(z)\eta\frac{\partial P}{\partial\eta}+\frac{R(z)^2\eta}{Re_f L_{dr}^2}\frac{\partial}{\partial\beta}\left(f_v\frac{\partial V}{\partial\beta}\right)$$
$$+\frac{1}{Re_f}\left\{2+\frac{\eta^2}{L_{dr}^2}\left[\frac{dR(z)}{d\beta}\right]^2\right\}\frac{\partial}{\partial\eta}\left(f_v\eta\frac{\partial V}{\partial\eta}\right)$$
$$-\frac{R(z)^2\eta^2}{Re_f L_{dr}^2}\frac{\partial}{\partial\beta}\left[\frac{f_v}{R(z)}\frac{dR(z)}{d\beta}\frac{\partial V}{\partial\eta}\right]-\frac{R(z)\eta^2}{Re_f L_{dr}^2}\frac{dR(z)}{d\beta}\frac{\partial}{\partial\eta}\left(f_v\frac{\partial V}{\partial\beta}\right)$$
$$+\frac{R(z)^2\eta^2}{Re_f L_{dr}^3}\frac{\partial}{\partial\beta}\left[f_v\frac{dR(z)}{d\beta}\frac{\partial U}{\partial\beta}\right]+\frac{R(z)^2\eta}{Re_f L_{dr}}\frac{\partial}{\partial\beta}\left(\frac{f_v}{R(z)}\frac{\partial U}{\partial\eta}\right)$$
$$-\frac{R(z)^2\eta^3}{Re_f L_{dr}^3}\frac{\partial}{\partial\beta}\left\{\frac{f_v}{R(z)}\left[\frac{dR(z)}{d\beta}\right]^2\frac{\partial U}{\partial\eta}\right\}$$
$$+\frac{R(z)^2\eta^2}{Re_f L_{dr}^3}\frac{\partial}{\partial\beta}\left[f_v\frac{d^2R(z)}{d\beta^2}U\right]-\frac{R(z)^2\eta^2}{Re_f L_{dr}^3}\frac{\partial}{\partial\beta}\left\{\frac{f_v}{R(z)}\left[\frac{dR(z)}{d\beta}\right]^2U\right\}$$
$$+\frac{1}{Re_f L_{dr}}\left\{2+\frac{\eta^2}{L_{dr}^2}\left[\frac{dR(z)}{d\beta}\right]^2\right\}\frac{dR(z)}{d\beta}\frac{\partial}{\partial\eta}\left(f_v\eta^2\frac{\partial U}{\partial\eta}\right)$$
$$-\frac{\eta^2}{Re_f L_{dr}}\frac{dR(z)}{d\beta}\frac{\partial}{\partial\eta}\left(f_v\frac{\partial U}{\partial\eta}\right)-\frac{R(z)\eta^2}{Re_f L_{dr}^3}\left[\frac{dR(z)}{d\beta}\right]^2\frac{\partial}{\partial\eta}\left(f_v\eta\frac{\partial U}{\partial\beta}\right)$$
$$+\frac{1}{Re_f L_{dr}}\left\{2+\frac{\eta^2}{L_{dr}^2}\left[\frac{dR(z)}{d\beta}\right]^2\right\}\frac{dR(z)}{d\beta}\frac{\partial}{\partial\eta}(f_v\eta U)$$
$$-\frac{R(z)\eta^2}{Re_f L_{dr}^3}\frac{dR(z)}{d\beta}\frac{d^2R(z)}{d\beta^2}\frac{\partial}{\partial\eta}(f_v\eta U)-\frac{2f_v}{Re_f L_{dr}}\frac{dR(z)}{d\beta}U-\frac{2f_v}{Re_f\eta}V \quad (18)$$

Energy equation:

$$\frac{1}{L_{dr}}\frac{\partial\lfloor R(z)^2\eta Uf_\rho f_{C_p}\theta\rfloor}{\partial\beta}+\frac{\partial\lfloor R(z)\eta Vf_\rho f_{C_p}\theta\rfloor}{\partial\eta}$$
$$=\frac{R(z)^2\eta}{Re_f Pr_f L_{dr}^2}\frac{\partial}{\partial\beta}\left(f_k\frac{\partial\theta}{\partial\beta}\right)+\frac{1}{Re_f Pr_f}\left(1+\frac{\eta^2}{L_{dr}^2}\left[\frac{dR(z)}{d\beta}\right]^2\right)$$
$$\times\frac{\partial}{\partial\eta}\left(f_k\eta\frac{\partial\theta}{\partial\eta}\right)-\frac{R(z)^2\eta^2}{Re_f Pr_f L_{dr}^2}\frac{\partial}{\partial\beta}\left[\frac{f_k}{R(z)}\frac{dR(z)}{d\beta}\frac{\partial\theta}{\partial\eta}\right]$$
$$-\frac{R(z)\eta^2}{Re_f Pr_f L_{dr}^2}\frac{dR(z)}{d\beta}\frac{\partial}{\partial\eta}\left(f_k\frac{\partial\theta}{\partial\beta}\right)$$
$$+2f_\rho f_v\frac{E_{vt}}{Re_f}\left\{\eta\left(\frac{\partial U}{\partial\eta}\right)^2+\frac{U^2}{\eta}+\eta\left\{\frac{R(z)\eta}{L_{dr}^2}\frac{\partial}{\partial\beta}\left[\frac{dR(z)}{d\beta}U\right]\right.\right.$$
$$\left.\left.-\frac{\eta}{L_{dr}^2}\left[\frac{dR(z)}{d\beta}\right]^2\frac{\partial}{\partial\eta}(\eta U)+\frac{R(z)}{L_{dr}}\frac{\partial V}{\partial\beta}-\frac{\eta}{L_{dr}}\frac{dR(z)}{d\beta}\frac{\partial V}{\partial\eta}\right\}^2\right\}$$
$$+\eta f_\rho f_v\frac{E_{vt}}{Re_f}\left[\frac{R(z)}{L_{dr}}\frac{\partial U}{\partial\beta}+\frac{1}{L_{dr}}\frac{dR(z)}{L_{dr}d\beta}U+\frac{\partial V}{\partial\eta}\right]^2 \quad (19)$$

Dopant diffusion equation:

$$\frac{1}{L_{dr}}\frac{\partial[R(z)^2\eta UC]}{\partial\beta}+\frac{\partial[R(z)\eta VC]}{\partial\eta}$$
$$=\frac{R(z)^2\eta}{PeL_{dr}^2}\frac{\partial}{\partial\beta}\left(f_D\frac{\partial C}{\partial\beta}\right)$$
$$+\frac{1}{Pe}\left\{1+\frac{\eta^2}{L_{dr}^2}\left[\frac{dR(z)}{d\beta}\right]^2\right\}\frac{\partial}{\partial\eta}\left(f_D\eta\frac{\partial C}{\partial\eta}\right)$$
$$-\frac{R(z)^2\eta^2}{PeL_{dr}^2}\frac{\partial}{\partial\beta}\left[\frac{f_D}{R(z)}\frac{dR(z)}{d\beta}\frac{\partial C}{\partial\eta}\right]$$
$$-\frac{R(z)\eta^2}{PeL_{dr}^2}\frac{dR(z)}{d\beta}\frac{\partial}{\partial\eta}\left(f_D\frac{\partial C}{\partial\beta}\right) \quad (20)$$

This set of equations applies to the preform and fiber in the drawing region. The equations for inert gas can be easily derived from Eqs. (16) to (19) by replacing η with $\frac{k_r-\eta}{k_r-1}$. Clearly, the dopant diffusion equation does not apply to inert gas, and the nondimensionalized form of the other governing equations for the inert gas can be derived from the nondimensionalized governing equations for preform/fiber by simple mathematical manipulation.

At the entrance to the furnace, the temperatures of the preform and the inert gas are taken as constant at room temperature. The axial velocities of the preform/fiber and inert gas are uniform, while the radial velocities are zero. The dopant concentration is expressed as mass fraction of the dopant, and is assumed to follow a step function as

$$c=\begin{cases}c_0 & \text{for } 0<\eta\leqslant 0.1\\ 0 & \text{for } 0.1<\eta\leqslant 1\end{cases} \quad (21)$$

where the initial dopant concentration in the preform core c_0 is set to 0.2 in this study.

The velocity normal to the interface of the preform/fiber and the inert gas is zero, while the velocity along the interface is continuous on both sides. Velocity is obtained by applying the continuity of shear stress at the preform/fiber–inert gas interface. The temperature is continuous and the heat flux satisfies the following condition:

$$\left(k\frac{\partial T}{\partial n}\right)_{\text{fiber}}=\left(k\frac{\partial T}{\partial n}\right)_{\text{gas}}+q_{\text{rad}} \quad (22)$$

where the radiation heat flux at the surface of the preform/fiber, q_{rad}, is computed using the same approach proposed by Lee and Jaluria [15]. The radiation heat transfer is studied using an enclosure model proposed by Lee and Jaluria [15], with the enclosure composed of furnace wall, outer surface of preform/fiber, and the inlet and outlet of the inert gas. The gas within the radiative enclosure is treated as nonparticipating. The furnace is taken as a diffuse gray

surface with a constant diffusivity of 0.75 [16]. The inlet and outlet of the inert gas are treated as black surfaces at an ambient temperature of 300 K. The silica preform is assumed to be a diffuse and spectral surface, and its hemispherical, spectral emissivity is represented by a fifth-order polynomial [15]:

$$\begin{aligned}\varepsilon &= 1.73734\times10^{-3}(2ar)^5 - 2.7\times10^{-2}(2ar)^3 \\ &\quad -0.545(2ar)^2 + 0.999788(2ar) \\ &\quad -4.3003\times10^{-3} \quad \text{for } 2ar \leqslant 5 \\ \varepsilon &= 0.8852646 \quad \text{for } 2ar \geqslant 5\end{aligned}$$

where the absorption coefficient, a, is obtained using the band approximation [4] assuming that outside of the band between 3 and 8 μm, the fiber is perfectly transparent. The absorption coefficient, a, for different wavelength, λ, is as follows: for $\lambda < 3$ μm and $\lambda > 8$ μm, $a = 0$; for 3.0 μm $< \lambda <$ 4.8 μm, $a = 400\ \mathrm{m}^{-1}$; and for 4.8 μm $< \lambda <$ 8.0 μm, $a = 15{,}000\ \mathrm{m}^{-1}$.

The radiative transport within the preform/fiber is taken into account using diffusion approximation. Under this approximation, the apparent thermal conductivity of the preform/fiber is the sum of the nonradiative conductivity, k_{cond}, and radiative conductivity, k_{rad}, expressed as

$$k_{\mathrm{rad}} = \frac{16n^2\sigma T^3}{3a} \tag{23}$$

where n is the refractive index of silica glass, σ the Stefan–Boltzmann constant, and a the absorption coefficient of silica glass.

Zero flux condition is applied to all the transport variables at the centerline of the preform/fiber. A fully developed condition is used for the flow and temperature for the inert gas at the outlet of the furnace.

2.2. Cooling region

When exiting the furnace, the fiber is near its melting temperature, and has to be cooled before coating can be applied. As seen in Fig. 1, the fiber is first cooled by natural convection to the surrounding air. However, in high speed drawing, natural convection alone is usually insufficient to lower the fiber temperature to the level required by the coating process, and supplemental cooling using forced convection is necessary. The governing equations in the cooling region are much simpler since the speed and radius of the fiber are constant; as a result, no coordinate or velocity transformation is needed in this region. The nondimensionalized governing equations for energy transport and dopant diffusion in the fiber are

Energy equation:

$$\frac{1}{L}\frac{\partial\theta}{\partial\beta} = \frac{1}{Re_{\mathrm{f}}Pr_{\mathrm{f}}}\left[\frac{1}{L^2}\frac{\partial}{\partial\beta}\left(\frac{\partial\theta}{\partial\beta}\right) + \frac{1}{\eta}\frac{\partial}{\partial\eta}\left(\eta\frac{\partial\theta}{\partial\eta}\right)\right] \tag{24}$$

Dopant diffusion equation:

$$\frac{1}{L}\frac{\partial C}{\partial\beta} = \frac{1}{Pe_{\mathrm{c}}}\left[\frac{1}{L^2}\frac{\partial}{\partial\beta}\left(\frac{\partial C}{\partial\beta}\right) + \frac{1}{\eta}\frac{\partial}{\partial\eta}\left(\eta\frac{\partial C}{\partial\eta}\right)\right] \tag{25}$$

Note that since the fiber is moving with a constant, known, velocity and further since there is no fluid motion within the fiber, continuity and momentum equations are not needed to describe the fiber domain. The governing equations for the surrounding cooling gas include the continuity, momentum, and energy equations as presented below in their nondimensional form

Continuity equation:

$$\frac{R_{\mathrm{c}}}{L}\frac{\partial U}{\partial\beta} + \frac{1}{\eta}\frac{\partial(\eta V)}{\partial\eta} = 0 \tag{26}$$

Momentum equations:

$$\begin{aligned}&\frac{R_{\mathrm{c}}}{L}\frac{\partial(f_\rho U^2)}{\partial\beta} + \frac{1}{\eta}\frac{\partial(f_\rho\eta UV)}{\partial\eta} \\ &\quad = -\frac{R_{\mathrm{c}}}{L}\frac{\partial P}{\partial\beta} + \frac{1}{Re_{\mathrm{c}}}\left[\left(\frac{R_{\mathrm{c}}}{L}\right)^2\frac{\partial}{\partial\beta}\left(f_\rho f_v\frac{\partial U}{\partial\beta}\right)\right. \\ &\qquad \left. + \frac{1}{\eta}\frac{\partial}{\partial\eta}\left(f_\rho f_v\eta\frac{\partial U}{\partial\eta}\right)\right]\end{aligned} \tag{27}$$

$$\begin{aligned}&\frac{R_{\mathrm{c}}}{L}\frac{\partial(f_\rho UV)}{\partial\beta} + \frac{1}{\eta}\frac{\partial(f_\rho\eta V^2)}{\partial\eta} \\ &\quad = -\frac{\partial P}{\partial\eta} + \frac{1}{Re_{\mathrm{c}}}\left[\left(\frac{R_{\mathrm{c}}}{L}\right)^2\frac{\partial}{\partial\beta}\left(f_\rho f_v\frac{\partial V}{\partial\beta}\right)\right. \\ &\qquad \left. + \frac{1}{\eta}\frac{\partial}{\partial\eta}\left(f_\rho f_v\eta\frac{\partial V}{\partial\eta}\right)\right] - \frac{f_\rho f_v V}{Re_{\mathrm{c}}\eta^2}\end{aligned} \tag{28}$$

Energy equation:

$$\begin{aligned}&\frac{R_{\mathrm{c}}}{L}\frac{\partial(f_\rho f_{C_p}U\theta)}{\partial X} + \frac{1}{\eta}\frac{\partial(f_\rho f_{C_p}\eta V\theta)}{\partial\eta} \\ &\quad = \frac{1}{Re_{\mathrm{c}}Pr_{\mathrm{c}}}\left[\left(\frac{R_{\mathrm{c}}}{L}\right)^2\frac{\partial}{\partial\beta}\left(f_k\frac{\partial\theta}{\partial\beta}\right) + \frac{1}{\eta}\frac{\partial}{\partial\eta}\left(f_k\eta\frac{\partial\theta}{\partial\eta}\right)\right]\end{aligned} \tag{29}$$

A prescribed convection coefficient in the range of 150–300 W/m^2 K [17] is applied to the fiber surface at the natural convective cooling region and the boundary conditions at the fiber/gas interface is given by

$$\frac{\partial\theta}{\partial\eta} = Bi(\theta_{\mathrm{inf}} - \theta); \quad Bi = \frac{hr_{\mathrm{f}}}{k_{\mathrm{f}}} \tag{30}$$

where Bi is the Biot number for natural convection as defined above.

For forced convective cooling, the gas enters the cooling tube with a uniform axial velocity at room temperature. A no slip condition is applied to the cooling gas at the wall, where constant room temperature is assumed. At the interface of the fiber and the cooling gas, a continuity condition is applied to the velocity and shear rate, temperature and heat flux, and a no-penetration condition is applied to the dopant concentration. At the outlet of the cooling region, the velocity, temperature and dopant concentration profiles are considered to be fully developed such that their axial gradients are zero. At the junction of the drawing region and cooling region of the fiber, a continuity

condition is applied to temperature, dopant concentration, heat flux and mass flux. The heat flux leaving the outlet interface of the drawing region through conduction equals the heat flux entering the inlet interface of the cooling region through conduction, and the dopant diffusion at the outlet interface of the drawing region equals the dopant diffusion at the inlet interface of the cooling region.

All the thermophysical properties of the preform/fiber, the inert gas, and the cooling gas are taken to be temperature dependent. In particular, for GeO_2 doped glass optical fiber, a few different diffusion coefficient equations are available in the literature. Among them the most widely used equation is the Arrhenius relation, which can be expressed as [27–29].

$$D = D_0 e^{-E/k_B T} \tag{31}$$

where D_0 is the inert diffusion constant, E is the activation energy, and k_B is the Boltzmann constant. The values of D_0 and E are obtained from the literature as $D_0 = 1.875 \times 10^4$ m^2/s and $E = 7.69 \times 10^4$ J.

The refractive index of the fiber can be expressed as a function of the dopant concentration using the Lorentz–Lorentz equation [30].

$$n = \sqrt{\frac{1+2\phi}{1-\phi}} \quad \text{and} \quad \phi = \frac{\sum \frac{(n_i^2-1)c_i}{(n_i^2+2)\rho_i}}{\sum \frac{c_i}{\rho_i}} \tag{32}$$

where n_i, c_i and ρ_i are the refractive index, mass fraction and density of component i, respectively. The refractive indices for pure SiO_2 and GeO_2 are 1.458 and 1.603, respectively [30].

The conservation equations of mass, momentum, energy, and species are coupled in the drawing region and cooling region since the properties of the preform/fiber and inert gas are all temperature dependent. Dopant diffusion introduces another layer of coupling since the properties of preform/fiber depend on the dopant concentration. For the purposes of this study, it is assumed that the effects of dopant concentration on the properties of preform/fiber are small, allowing for a decoupling of the energy and momentum equations from the dopant diffusion equation.

A control volume based finite difference method is used to solve the governing equations and boundary conditions. A nonuniform grid mesh was used in the entire computational domain, and a staggered grid structure was used in solving the Navier–Stokes equations to avoid unrealistic velocity solutions. The power law scheme [31] was used to represent the transport properties on the control volume surfaces, and a SIMPLER algorithm was adopted to solve the Navier–Stokes equations [31]. The coupled flow and temperature field in the drawing and the cooling regions were solved for using the following procedure: (a) an initial temperature and velocity fields were assumed for the preform/fiber, inert gas and cooling gas in the drawing and cooling regions; (b) the temperature and velocity in the preform/fiber and inert gas in the drawing region were solved for using the governing equations; (c) the temperature and velocity at the interface of the preform/fiber and inert gas were determined using the boundary conditions; (d) the temperature of the fiber was solved for in the natural convective cooling region; (e) the temperature of the fiber and cooling gas, and the velocity of the cooling gas were solved for in forced convective cooling region; (f) the temperature at the interface of the fiber and cooling gas was solved for in forced convective cooling region; (g) the temperature at the junctions of drawing and natural convective cooling, and natural and forced convective cooling region was determined; (h) the temperature and velocity fields for all the regions were updated; and (i) steps (b)–(h) were repeated until convergence.

The temperature and velocity field obtained were used to solve for the dopant concentration. The governing equations in the drawing and the cooling regions differ significantly in terms of complexity due to the large variation in radius in the drawing region, therefore the computation is carried out in two separate regions simultaneously, and is coupled as follows: (a) an initial dopant concentration is assumed at the interface of drawing and cooling regions; (b) the dopant concentration is solved for in the drawing region; (c) the dopant concentration is obtained in the cooling region; (d) the dopant concentration at the interface of drawing and cooling regions is updated using the continuity conditions in dopant concentration and mass flux; and (e) steps (b)–(d) are repeated until convergence. The converged solution is used in Eq. (32) to get the refractive index profile in the fiber. In all the calculations, the convergence criterion of the numerical solution for the temperature, velocity and dopant concentration fields was that the relative errors between two consecutive iterations are less than 10^{-7}.

Table 1
Typical mesh grids for (a) velocity, temperature, and (b) dopant diffusion fields

(a) For velocity and temperature fields	Drawing region		Natural cooling region	Forced cooling region	
	Preform/fiber	Inert gas	Fiber	Fiber	Cooling gas
Number of grids in axial direction	102	102	42	82	82
Number of grids in radial direction	42	62	18	18	22

(b) For dopant diffusion field	Drawing region	Natural cooling and forced cooling regions
Number of grids in axial direction	102	202
Number of grids in radial direction	102	36

To best capture the evolution of the temperature, the velocity, and the dopant concentration fields while minimizing computational effort, different grid schemes were used in discretizing these fields. Linear interpolation was used to obtain the temperature and velocity values under the different grid scheme in solving the dopant concentration equations. For the parametric study described in the following section, a typical number of mesh grids is shown in Table 1. For the cases studied, the total computation time for a typical case was about 20 h on a *SPARCstation* 10 *UNIX* machine with a single processor.

3. Results and discussion

The formulation in the previous section described the governing equations and boundary conditions representing the mass, momentum and energy transport in the preform/fiber, inert gas and cooling gas during the drawing and cooling steps of an optical fiber drawing process. The overall goal of the analysis is to predict the dopant concentration distribution and refractive index in the optical fiber. The computational results obtained from the analysis are presented in this section. The model is first verified by comparison with existing data in the open literature. With the validated model as basis, parametric studies are reported to elucidate the effects of several nondimensional parameters on the thermal and mass transport during the processes.

Since no numerical or experimental results are available in the open literature on dopant diffusion in the drawing and cooling regions or on conjugate temperature field in the combined drawing and cooling regions, the validation is limited only to the temperature field for individual drawing and cooling processes. For the drawing region, the surface temperature is compared with numerical data from Choudhury and Jaluria [8]. The result is shown in Fig. 2a, in which the neck-down shape of the fiber is the same as that described in the previous section, the radius and surface temperature of the furnace are 1.9 cm and 2500 K, respectively, and the inert gas is air with an inlet velocity of 5.2824 cm/s. Fig. 2a shows that in the upper neck-down region, the temperature increases rapidly from the ambient temperature to near the furnace temperature, and remains essentially constant through the neck-down region. Overall, the current model prediction is seen to compare well with the simulation results of Choudhury and Jaluria [8] throughout the domain.

For the cooling region, the present simulations were compared with results obtained by Choudhury et al. [5] for a glass fiber cooled by helium, and the result is shown in Fig. 2b. In this process, the diameter of the fiber is 150 μm, and the speed of the fiber is 1.67 m/s. The initial temperature of the fiber at the entrance is uniform, and the length and width of the cooling channel are 5 and 600 times of the fiber radius, respectively. The velocity of the cooling gas, helium, is twice the fiber speed at the entrance. In the figure, the temperature is defined as

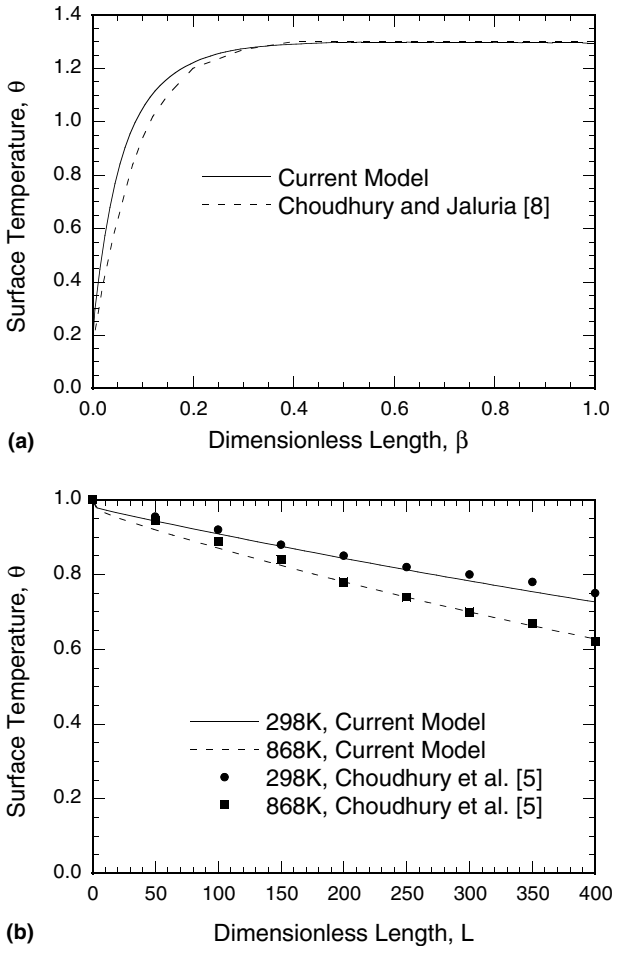

Fig. 2. (a) A comparison of the surface temperature profile in the furnace region predicted by the present model and available numerical data for an optical fiber drawing process, and (b) a comparison of the surface temperature decay predicted by the present model and available numerical data for an optical fiber cooling process.

$\theta = \frac{T-T_\infty}{T_0-T_\infty}$, where the fiber temperature at the entrance, T_0, is set to be 868 K, and the ambient temperature, T_∞ is set to be 300 K. The dimensionless distance is defined as $L = \frac{z}{r_f}$. Here comparisons were made for constant properties taken at two different temperatures, 298 K and 868 K, respectively. Fig. 2a and b show that the results of the current model are in close agreement with those available in the open literature.

The validated simulation model was used to investigate the effects of several nondimensional parameters on the mass, momentum and thermal transport during the drawing and cooling of optical fibers in order to determine the dominant parameters and their physical effects on the process. The ranges of nondimensional groups used are based on typical practical situations for fiber drawing and cooling. The results on temperature and dopant distributions are presented and discussed; however velocity fields are omitted here in the interest of brevity. For all the results shown, unless otherwise specified, the following conditions are employed: The properties of the fiber and gas are taken

to be temperature dependent. The reference temperature for fiber and inert gas is the fiber melting temperature, 1900 K, while the reference temperature for cooling gas is taken as ambient temperature, 300 K. The fiber velocity is 3 m/s, and the inert gas velocity at entrance is 200 times that of the preform velocity. The entrance temperature for preform, inert gas and cooling gas is 300 K. The width of the cooling channel is 0.8 cm, and the lengths of the natural and forced convective cooling section are 0.5 m and 1 m, respectively. The convective coefficient is taken as 300 W/m^2 K. The inert gas is taken as air, and the cooling gas is taken as helium. The nondimensional groups used in the parametric study presented in Figs. 3–11 are as follow: $Re_f = 1 \times 10^{-7}$, $Re_a = 300$, $Re_c = 500$, $R_F = 400$, $\theta_F = 1.2105$, $Bi = 0.0053$, $R_c = 200$, $K_{c,f} = K_c/K_f = 0.04$, and $Pe = 7.28 \times 10^9$, unless otherwise noted in the figures.

3.1. Effects of fiber Reynolds number

The effect of fiber Reynolds number on the temperature field, dopant concentration distribution, and refractive index profile is examined first. Three different fiber Reynolds numbers, 4×10^{-8}, 1×10^{-7}, and 2×10^{-7}, are considered. Fig. 3 shows the surface temperature (Fig. 3a) and centerline dopant concentration (Fig. 3b) as a function of dimensionless length, β, and the refractive index profile as a function of dimensionless radius, η, in Fig. 3c. The surface temperature decays exponentially in the natural convective cooling region, as shown in Fig. 3a. In the forced convective cooling region, the surface temperature drops rapidly near the entrance because of a high convective coefficient and large temperature difference between the fiber and the cooling gas. The surface temperature decay slows down along the cooling channel because of the decreasing temperature difference between the fiber and cooling gas. Fig. 3b shows that the dopant concentration at the centerline of the fiber remains essentially constant at the upper neck-down region. This is due to the fact that the diffusion coefficient is very small at low temperatures. The centerline dopant concentration starts decreasing when the temperature increases.

As the fiber Reynolds number increases, the fiber remains in the furnace for a shorter time and, therefore, the temperature rise is slower and smaller, as evident from Fig. 3a. Similarly, a shorter residence time in the cooling region results in a slower surface temperature decay. It follows that when the fiber Reynolds number exceeds a certain value, the fiber temperature will not be able to rise to above its melting point and therefore, the drawing process will not be able to take place. On the other hand, more effective cooling techniques have to be resorted to at high fiber Reynolds numbers. Fig. 3b shows that dopant diffusion decreases with fiber Reynolds number. This is due to the decreasing dopant diffusion coefficient as a result of the decreasing temperature, and the shorter time period for diffusion. Fig. 3c shows the refractive index profile in the final fiber, and illustrates two important properties:

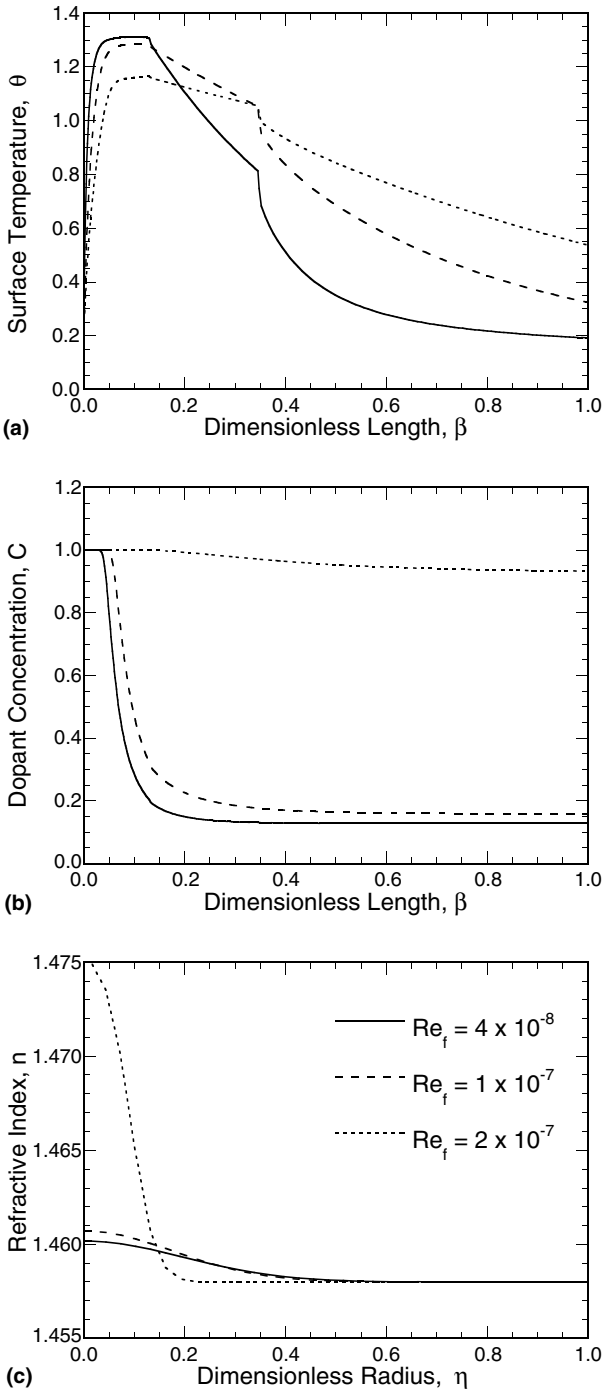

Fig. 3. Effects of fiber Reynolds number on (a) preform/fiber surface temperature, (b) preform/fiber centerline dopant concentration decay, and (c) fiber refractive index profile.

the maximum refractive index difference between the core and cladding increases with fiber Reynolds number, and consequently, the core radius decreases with fiber Reynolds number.

3.2. Effects of inert gas Reynolds number

Fig. 4 represents the effect of inert gas Reynolds number on the surface temperature, centerline dopant

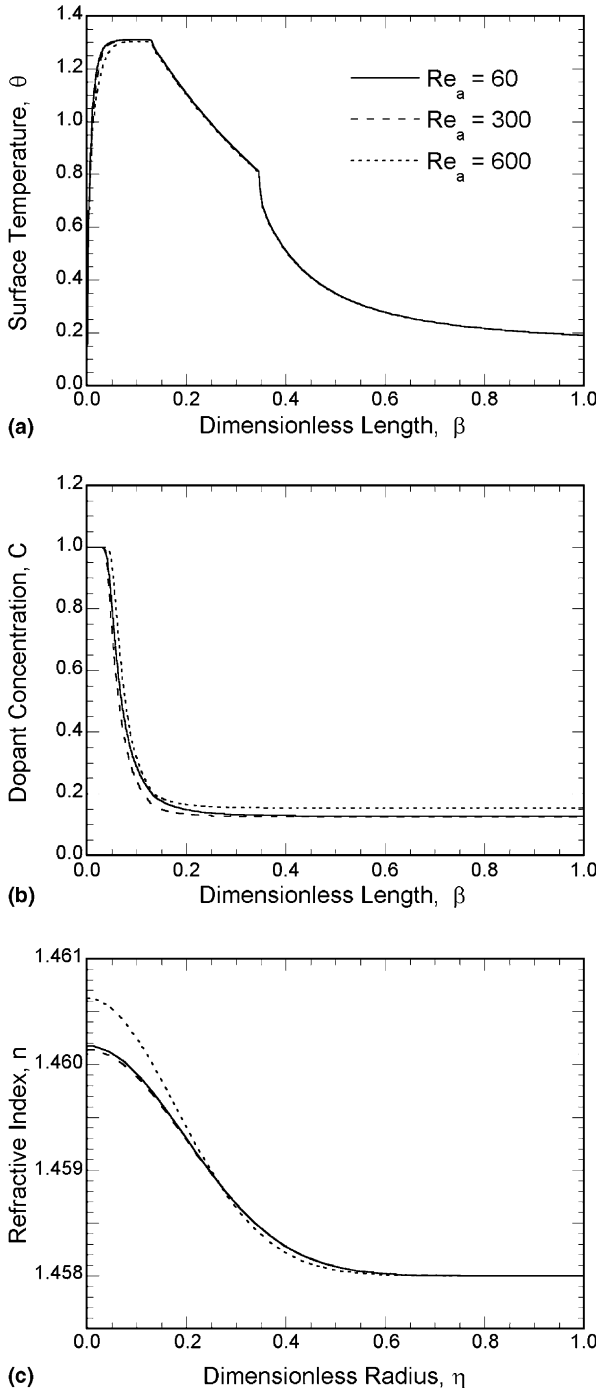

Fig. 4. Effects of inert gas Reynolds number on (a) preform/fiber surface temperature, (b) preform/fiber centerline dopant concentration decay, and (c) fiber refractive index profile.

concentration, and refractive index profile of the fiber. Three different inert gas Reynolds numbers, 60, 300 and 600, are examined. For the cases studied, as the Reynolds number of the inert gas increases, fiber surface temperature in the drawing region decreases, as seen in Fig. 4a. However, as the inert gas Reynolds number gets smaller, this effect gets smaller and the surface temperature is hardly affected by the inert gas Reynolds number. When air is used as the inert gas, the surface temperature of the fiber is higher than that of the adjacent inert gas, and therefore, the inert gas absorbs heat from the fiber. The amount of heat absorbed by the inert gas increases with the inert gas Reynolds number due to the increased convection, and consequently, the surface temperature of the fiber decreases with the inert gas Reynolds number. However, since the dominant mode of heat transfer in the furnace is the radiation between the fiber and furnace wall, the effect of convection decreases as the Reynolds number of the inert gas decreases. When the inert gas Reynolds number is small enough, the surface temperature of the fiber becomes essentially independent of the convective heat transfer between the fiber and the inert gas. Fig. 4a also shows that the effect of the inert gas Reynolds number on the fiber surface temperature is restricted in the drawing region, namely, the temperature decay in the cooling region is hardly affected by the Reynolds number of the inert gas.

Fig. 4b shows the centerline dopant concentration for three different Reynolds numbers of the inert gas. As seen, the inert gas Reynolds number has an interesting effect on the centerline dopant concentration. As the Reynolds number of the inert gas increases, the centerline dopant concentration decreases at first, but starts increasing when the inert gas Reynolds number is increased further. This is due to the complex effect of the inert gas Reynolds number on the temperature field. As the Reynolds number of the inert gas increases, the centerline temperature of the fiber also decreases, but the temperature difference between the surface and the centerline may decrease or increase depending on the axial location of the fiber, which again, affects the dopant diffusion. Fig. 4c represents the refractive index profile for three different inert gas Reynolds numbers. Little difference exists for $Re_a = 60$ and $Re_a = 300$, while the maximum refractive index difference between the core and the cladding is higher for $Re_a = 600$.

3.3. Effects of cooling gas Reynolds number

The effect of cooling gas Reynolds number is investigated using three different values of 100, 500 and 1000. As seen in Fig. 5a, the effect of cooling gas Reynolds number on the fiber surface temperature field is restricted to the forced convective cooling region, which suggests that the heat transfer in the cooling region is dominated by advection due to the large speed and relatively low thermal conductivity of the fiber. As the cooling gas Reynolds number increases, the fiber surface temperature decay becomes rapid due to an increase in the local Nusselt number, but as the cooling gas Reynolds number increases further, temperature decay starts decreasing. This can be explained as follows: although the local Nusselt number increases with the cooling gas Reynolds number, the temperature of the adjacent cooling gas also rises, which results in an overall effect of decreasing heat transfer, and therefore, a decrease in the surface temperature decay. For the cases studied, as seen in Fig. 5b and c, the effects of cooling gas Reynolds number on the centerline dopant concentration and the

final refractive index profile are very small. When the cooling gas Reynolds number increases from 100 to 1000, the centerline dopant concentration increases slightly, as does the maximum refractive index difference between the core and cladding of the fiber. No distinguishable difference exists in centerline dopant concentration and final refractive index profile when the cooling gas Reynolds number varies from 100 to 500.

3.4. Effects of furnace radius

Fig. 6 shows the effect of furnace radius on the surface temperature (Fig. 6a), centerline dopant concentration (Fig. 6b), and refractive index profile of the fiber (Fig. 6c). Three different dimensionless furnace radii, 300, 400, and 500, are examined. When the furnace radius increases, the view factor of the fiber with respect to the

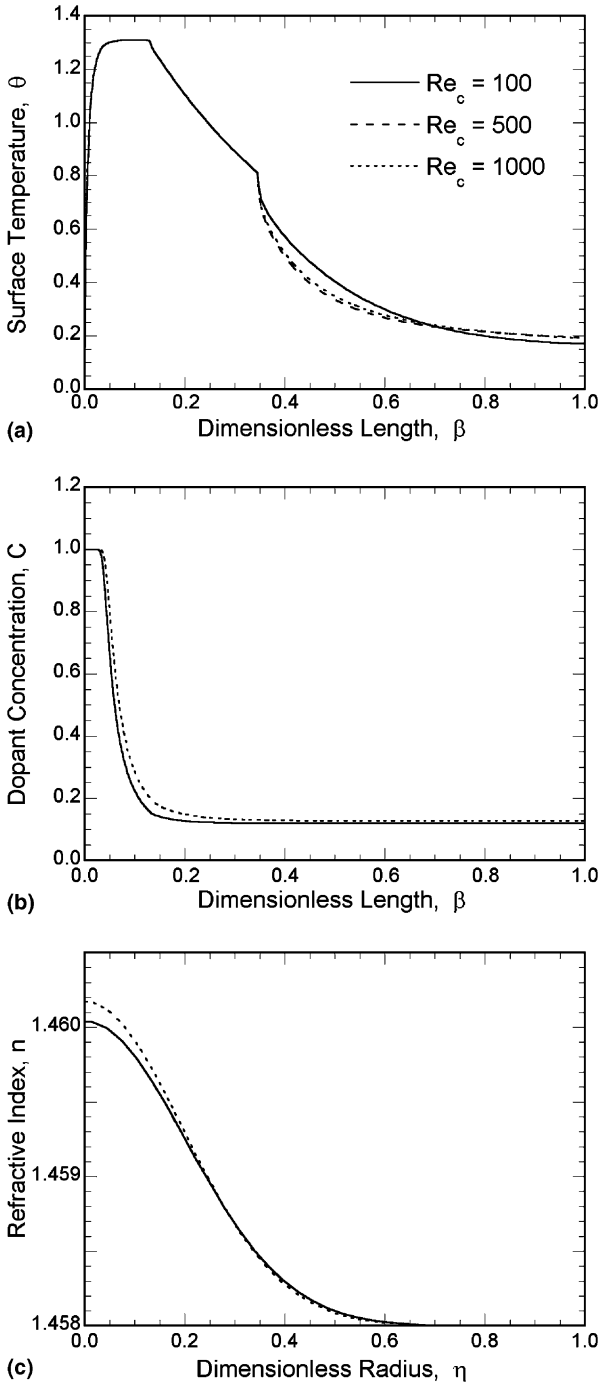

Fig. 5. Effects of cooling gas Reynolds number on (a) preform/fiber surface temperature, (b) preform/fiber centerline dopant concentration decay, and (c) fiber refractive index profile.

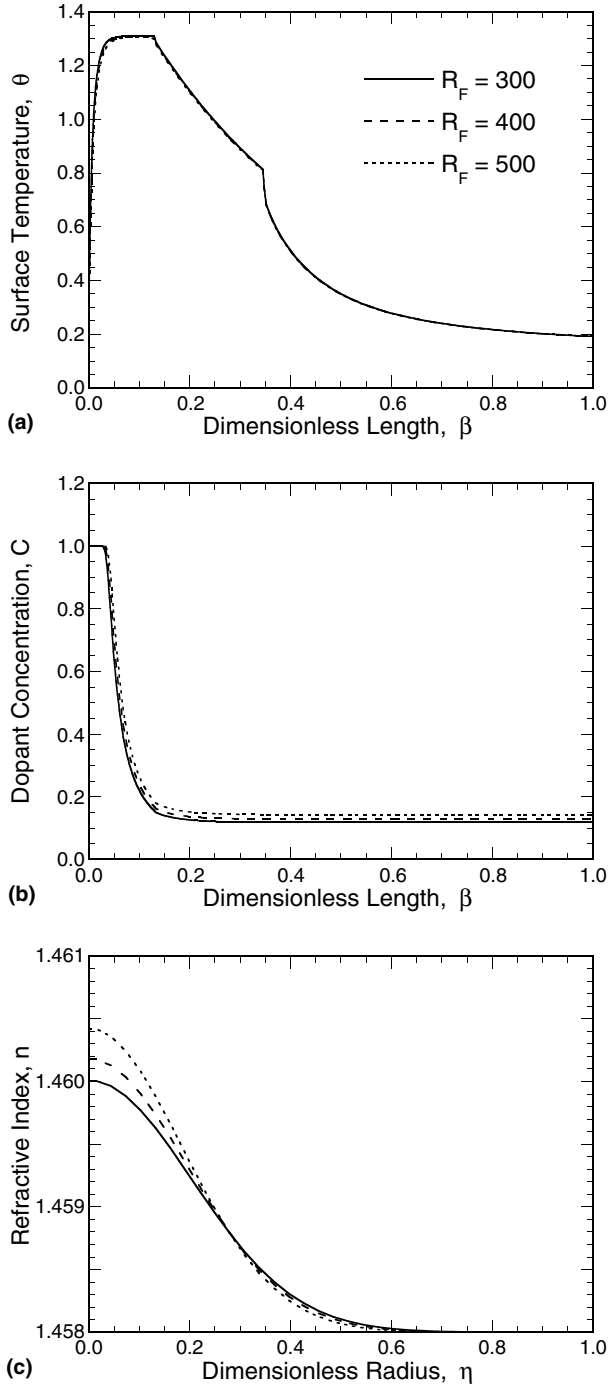

Fig. 6. Effects of furnace radius on (a) preform/fiber surface temperature, (b) preform/fiber centerline dopant concentration decay, and (c) fiber refractive index profile.

furnace is decreased slightly. This results in a smaller radiation transport between the furnace and the preform/fiber, which, in turn, decreases the surface temperature of the preform/fiber. The volumetric flow rate of the inert gas also increases because of the larger furnace radius, enhancing the convection transport between the preform/fiber and the inert gas. This again results in a decrease in the surface temperature of the preform/fiber. However, the magnitude of the effect of furnace radius on the surface temperature is very small in the cases studied, as seen in Fig. 6a. Fig. 6b shows that the centerline dopant concentration decay decreases with the furnace radius, due to a decrease of the diffusion coefficient resulting from a reduced fiber temperature. Fig. 6c shows that the maximum refractive index difference between the core and cladding of the fiber increases with the furnace radius because of the decreased dopant diffusion.

3.5. Effects of furnace wall temperature

In order to investigate the effect of furnace wall temperature, three different levels of constant furnace wall temperature were examined, i.e., 2100 K, 2300 K and 2500 K, or 1.1053, 1.2105 and 1.3158, in dimensionless form. As shown in Fig. 7a and b, the furnace wall temperature has a strong effect on the temperature and dopant concentration distribution of the fiber. As the furnace wall temperature increases, Fig. 7a shows that the surface temperature of the fiber increases due to the increased radiation transport between the preform/fiber and the furnace wall. This results in an increase in the dopant diffusion, which is represented by greater decay in the centerline dopant concentration as seen in Fig. 7b. Consequently, Fig. 7c indicates that the gradient of refractive index within the core of the fiber decreases. When the furnace wall temperature is very low, the dopant diffusion becomes very small, and the final refractive index of the fiber takes essentially the same profile as that of the preform.

3.6. Effects of Biot number of natural convection

The effect of the Biot number of natural convective cooling is shown by considering three different Biot numbers, 0.0027, 0.0053 and 0.0080. As shown in Fig. 8a, the effect of Biot number on temperature distribution is felt only in the cooling region. As expected, the temperature decays faster with the increasing Biot number of the natural convective cooling. Fig. 8b shows the effect of Biot number on the dopant concentration; as the Biot number increases, the dopant concentration also increases due to a decrease in the dopant diffusion due to the increasing Biot number. The maximum refractive index difference between the core and the cladding increases with the Biot number of the natural convective cooling because of the reduced dopant diffusion, as seen in Fig. 8c.

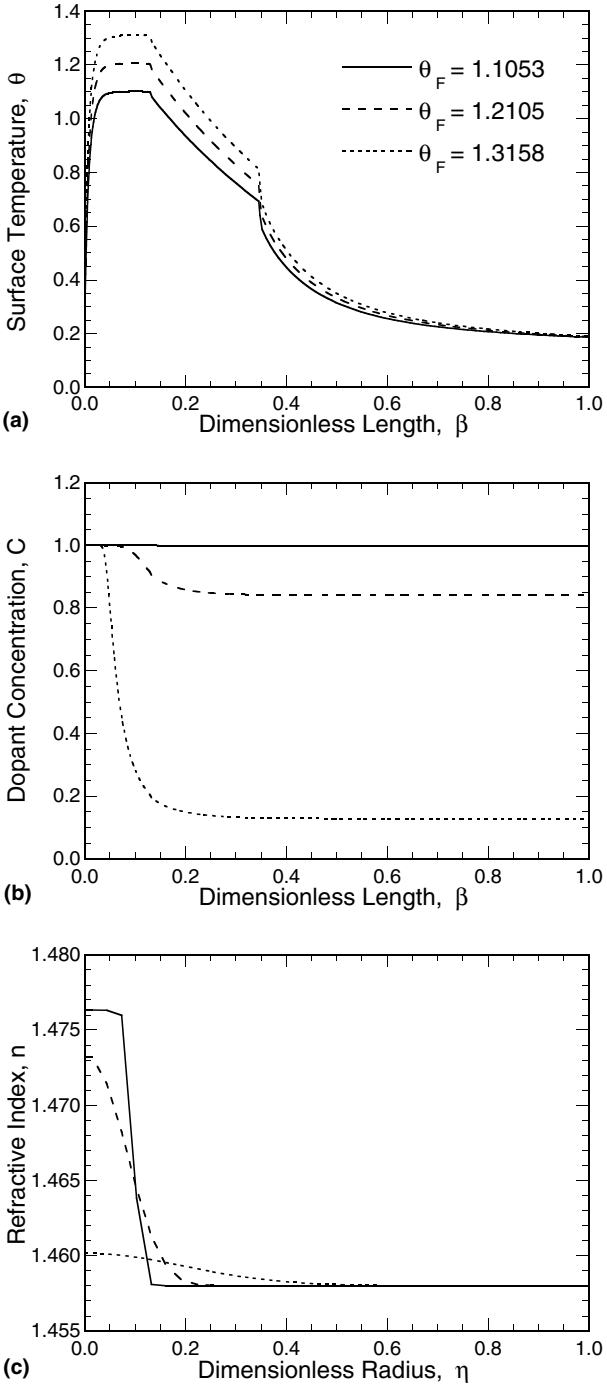

Fig. 7. Effects of furnace wall temperature on (a) preform/fiber surface temperature, (b) preform/fiber centerline dopant concentration decay, and (c) fiber refractive index profile.

3.7. Effects of cooling channel radius

Fig. 9 shows the effect of cooling channel radius for three different dimensionless cooling channel radii, i.e., 100, 200, and 400. Fig. 9a shows that as the cooling channel radius decreases, the temperature gradient at the surface increases resulting in greater temperature decay near the entrance of the forced cooling. This effect is reversed toward the end of the cooling channel due to a decreased

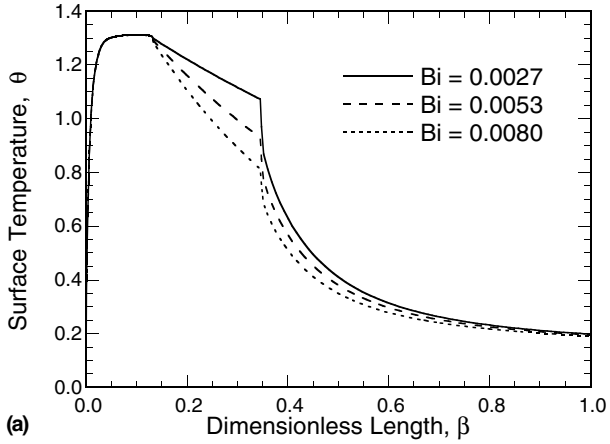

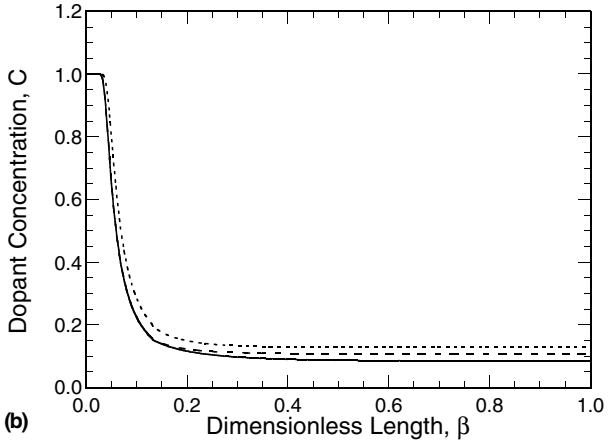

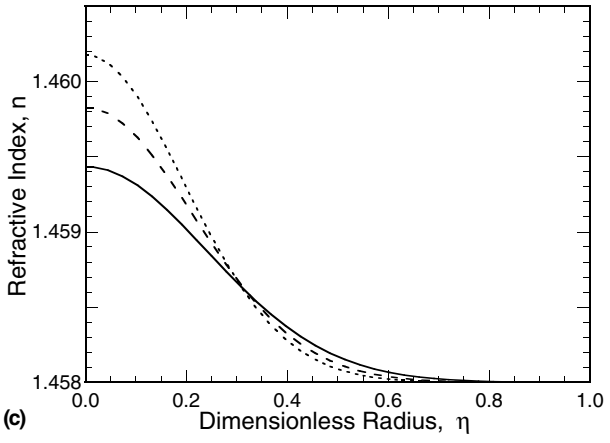

Fig. 8. Effects of Biot number of natural convective cooling on (a) preform/fiber surface temperature, (b) preform/fiber centerline dopant concentration decay, and (c) fiber refractive index profile.

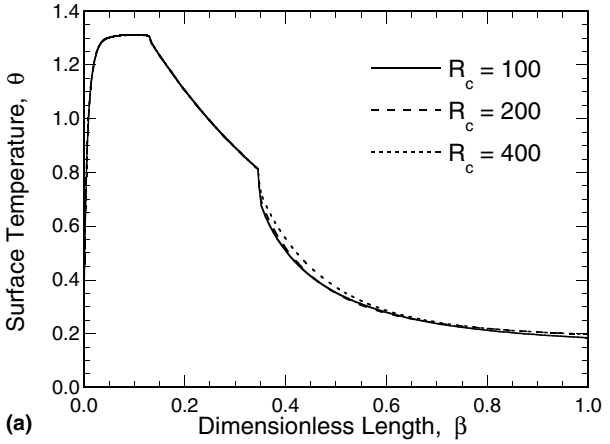

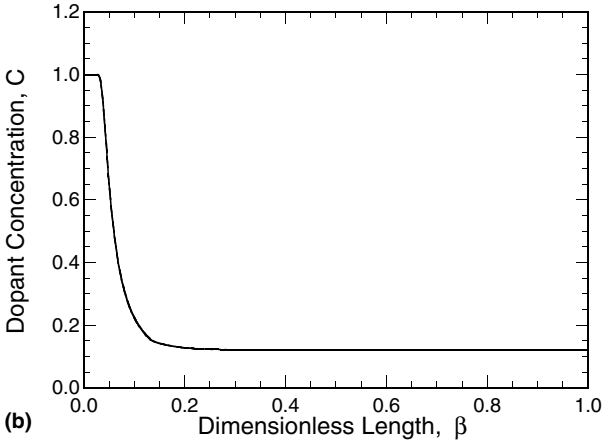

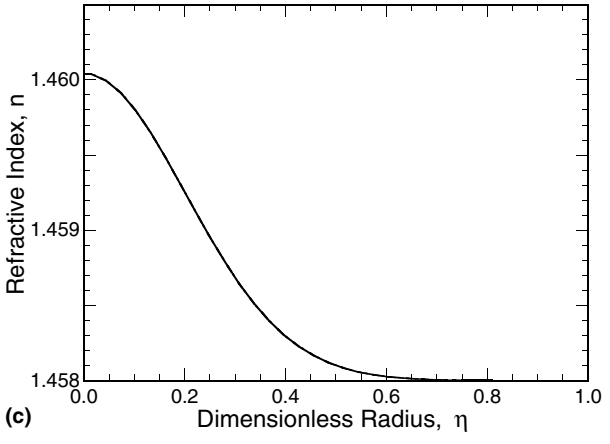

Fig. 9. Effects of cooling channel radius on (a) preform/fiber surface temperature, (b) preform/fiber centerline dopant concentration decay, and (c) fiber refractive index profile.

temperature gradient resulting from the temperature rise in the cooling gas. The overall effect of cooling channel radius on the temperature distribution is seen to be small within the range studied. Although cooling channel radius has some effect on the temperature distribution in the forced convective cooling region, its effect on the dopant diffusion is minimal as noted in Fig. 9b. Since the dopant diffusion coefficient is very small for low temperatures, which is the case for the forced convective cooling region, the dopant diffusion is hardly affected by the cooling channel radius. Similarly, the final refractive index profile of the fiber is also relatively unaffected by the cooling channel radius, as seen in Fig. 9c.

3.8. Effects of cooling gas thermal conductivity

The effect of cooling gas properties is investigated by considering three different cooling gas thermal

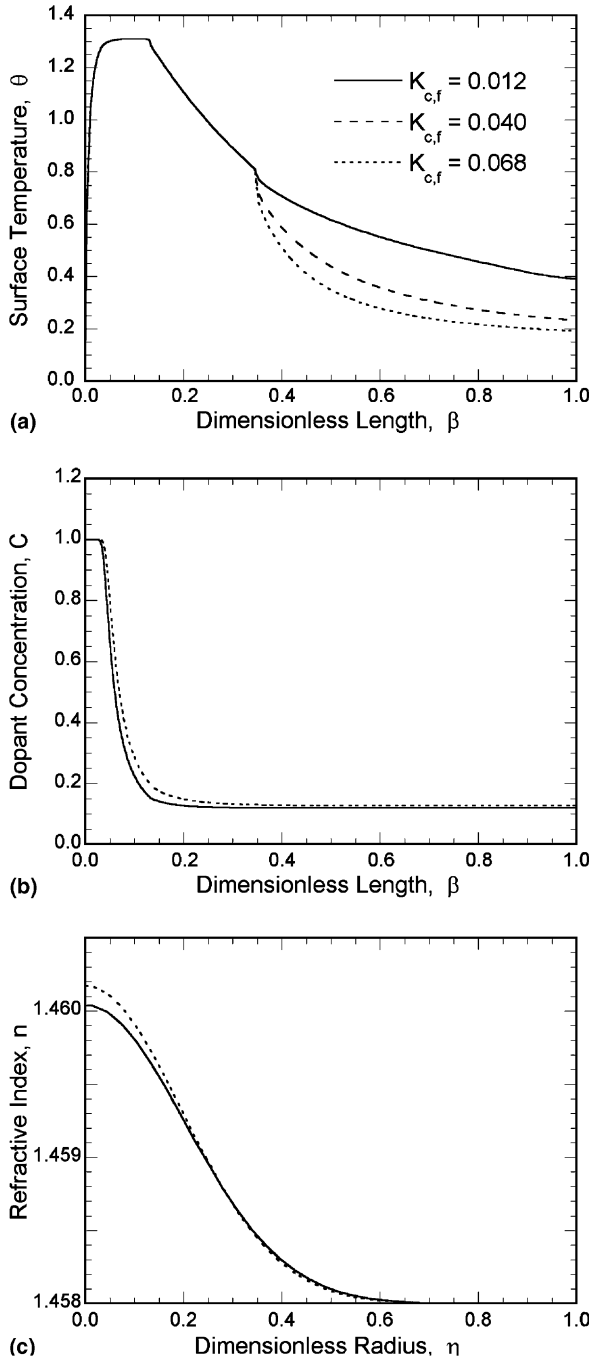

Fig. 10. Effects of cooling channel thermal conductivity on (a) preform/fiber surface temperature, (b) preform/fiber centerline dopant concentration decay, and (c) fiber refractive index profile.

conductivities, 0.012, 0.040, and 0.068, in dimensionless form defined as $K_{c,f} = \frac{k_c}{k_f}$. As the cooling gas thermal conductivity increases, the surface temperature decay in the fiber increases. This is because the thermal diffusion within the cooling gas is much stronger for larger cooling gas thermal conductivity. This suggests that different cooling fluids can be used to control the cooling rate. Although cooling gas thermal conductivity has a significant effect on the surface temperature decay in the forced convective region, its effect on the dopant diffusion is very small due to the small dopant diffusion coefficient at low temperatures. As seen in Fig. 10b, decreasing the cooling gas thermal conductivity increases the centerline dopant concentration decay slightly; however, the centerline dopant concentration decay remains unchanged when the cooling gas thermal conductivity is decreased further. This analysis also applies to the final refractive index profile of the fiber, whose results are shown in Fig. 10c.

3.9. Effects of dopant Peclet number

The effect of dopant properties is examined by considering three different dopant Peclet numbers, 3.64×10^9, 7.28×10^9, and 3.62×10^{10}, and the results are shown in Fig. 11. Since it has been assumed that the flow and temperature fields are not affected by the dopant, the surface temperature is independent of the dopant Peclet number, as seen in Fig. 11a. Fig. 11b shows that the centerline dopant concentration decay increases with the dopant Peclet number, as expected. The maximum refractive index between the core and the cladding of the fiber increases with the dopant Peclet number as shown in Fig. 11c; consequently, the core radius of the fiber decreases with dopant Peclet number. This suggests that different dopant can be used to achieve the desired refractive index profile.

The results in this section provide a comprehensive analysis of the effects of various nondimensional groups on the evolution of the fiber surface temperature, dopant concentration, and index of refraction profile during the optical fiber manufacturing process. The results could be used as guidelines in analyzing and designing for the final index of refraction profile while simultaneously satisfying other quality constraints. In a future work, optimum parameter combinations for specific design specifications will be determined by integrating the present model with a numerical optimization procedure. In the present study, the neck-down shape of the preform/fiber is approximated as a specified profile in the interest of minimizing computational effort; a more accurate neck-down shape during a drawing process could be solved for by performing a force balance at the preform/fiber surface. Further simplification of the numerical computation resulted from a decoupling of the temperature and velocity fields from the dopant concentration in the solution procedure. It was assumed that presence of dopant does not alter the thermophysical properties significantly, while the temperature, velocity and dopant concentration fields need to be solved together as a conjugate problem for an exact simulation. An effective use of physics-based models for practical design calls for incorporation of the inherent parameter uncertainty in a manufacturing environment into the simulations. To this end, stochastic modeling and analysis under uncertainty is presently being developed and will be reported in a forthcoming publication.

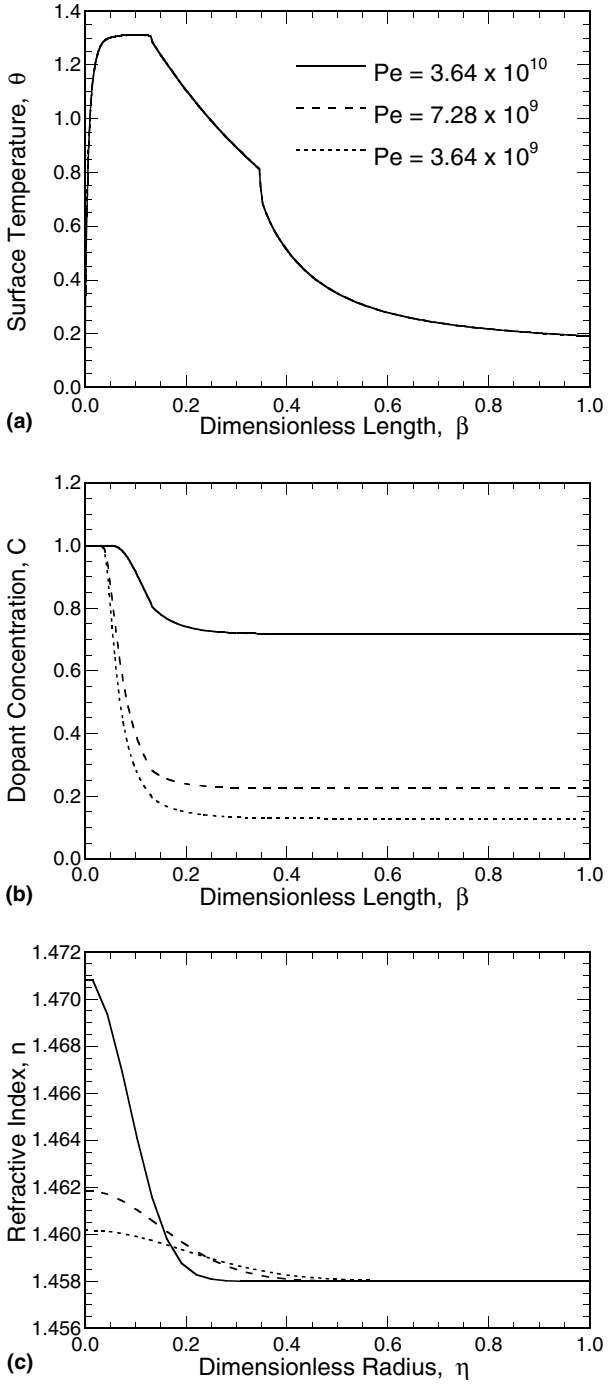

Fig. 11. Effects of dopant Peclet number on (a) preform/fiber surface temperature, (b) preform/fiber centerline dopant concentration decay, and (c) fiber refractive index profile.

4. Conclusions

In this study, a detailed numerical investigation on the flow, heat and mass transfer phenomena in the drawing and cooling process of glass optical fibers has been carried out using a finite difference approach based on primitive variables. A prescribed neck-down profile based on experimental results in the literature has been used, and a coordinate transformation is employed in the drawing process, with the use of covariant curvilinear velocity.

Different nondimensional parameters, namely the Reynolds numbers of fiber, inert and cooling gas, radius of furnace and cooling channel, furnace wall temperature, Biot number of natural convective cooling, cooling gas thermal conductivity and dopant Peclet number, were varied to investigate their effects on the thermal and mass transport during the drawing and cooling process of optical fiber. Based on the results and discussion presented above, it is found that the fiber Reynolds number, the furnace wall temperature and the dopant Peclet number have significant influence on the temperature field, dopant concentration distribution and refractive index profile, while the Reynolds numbers of inert and cooling gas, radius of furnace and cooling channel, Biot number of natural convective cooling and cooling gas thermal conductivity have minor effects. The results provide valuable insight for optimization of the process for tailored index of refraction profiles.

Acknowledgements

The work reported in this paper was funded by the National Science Foundation Information Technology Research (ITR) program through Grant No. CTS-0112822. We gratefully acknowledge the support. The authors also acknowledge the help of Dr. Andryas Mawardi in the preparation of the manuscript.

References

[1] R. Olshansky, Pulse broadening caused by deviations from the optimal index profile, Appl. Opt. 15 (1976) 782–788.
[2] H.M. Presby, D.M. Marcuse, W.G. French, Refractive-index profiling of single-mode optical fibers and preforms, Appl. Phys. 18 (23) (1979) 4006–4011.
[3] J. Kirchhof, P. Kleinert, A. Funke, B. Knappe, H.R. Muller, About the smoothing of concentration fluctuations by diffusion in the glass systems SiO_2/GeO_2 and $SiO_2/GeO_2/B_2O_3$, Cryst. Res. Technol. 22 (1987) K105–K108.
[4] M.R. Myers, A model for unsteady analysis of preform drawing, AIChE J. 35 (4) (1989) 592–602.
[5] S.R. Choudhury, Y. Jaluria, T. Vaskopoulos, C.E. Polymeropoulos, Forced convective cooling of optical fiber during drawing process, ASME J. Heat Transfer 116 (1994) 790–794.
[6] X. Cheng, Y. Jaluria, Effect of draw furnace geometry on high-speed optical fiber manufacturing, Numer. Heat Transfer Part A 41 (2002) 757–781.
[7] S.R. Choudhury, Y. Jaluria, Practical aspects in the drawing of an optical fiber, J. Mater. Res. 13 (2) (1998) 483–493.
[8] S.R. Choudhury, Y. Jaluria, Thermal transport due to material and gas flow in a furnace for drawing an optical fiber, J. Mater. Res. 13 (2) (1998) 494–503.
[9] S.R. Choudhury, Y. Jaluria, S. Lee, A computational method for generating the free-surface neck-down profile for glass flow in optical fiber drawing, Numer. Heat Transfer Part A 35 (1999) 1–24.
[10] Y. Dogu, D.A. Kaminski, Effects of eccentricity on glass temperatures in the neck-down stage of the optical fiber drawing process, in: Proceedings of the ASME Heat Transfer Conference, HTD-Vol 351, 1997, pp. 89–100.

[11] L.R. Glicksman, The cooling of glass fibres, Glass Technol. 9 (5) (1968) 131–138.
[12] M.G. Gossiaux, J.F. Bourhis, G. Orcel, Numerical simulation of optical fiber cooling during the drawing process, in: International Wire and Cable Symposium Proceedings, 1998, pp. 81–84.
[13] D.A. Kaminski, Thermal transport in optical fiber manufacturing, in: Proceedings of the First International Symposium on Radiation Transfer, 1995, pp. 667–681.
[14] B.H. Kang, Y. Jaluria, M.V. Karwe, Numerical simulation of conjugate transport from a continuous moving plate in materials processing, Numer. Heat Transfer Part A 19 (1991) 151–176.
[15] S.H.-K. Lee, Y. Jaluria, Effects of variable properties and viscous dissipation during optical fiber drawing, ASME J. Heat Transfer 118 (1996) 350–358.
[16] U.C. Paek, R.B. Runk, Physical behavior of the neck-down region during furnace drawing of optical fibers, J. Appl. Phys. 49 (1978) 4417–4422.
[17] U.C. Paek, Free drawing and polymer coating of silica glass optical fibers, ASME J. Heat Transfer 121 (1999) 774–788.
[18] D.S. Vaidya, G.D. Mihalacopoulos, Characterization of meltdown profile during fiber draw, in: International Wire and Cable Symposium Proceedings, 1998, pp. 73–80.
[19] V.N. Vasiljev, G.N. Dunlev, V.D. Naumchic, The flow of a highly viscous liquid with a free surface, Glass Technol. 30 (2) (1989) 83–90.
[20] Z. Yin, Y. Jaluria, Thermal transport and flow in high-speed optical fiber drawing, ASME J. Heat Transfer 120 (1998) 916–930.
[21] Z. Yin, Y. Jaluria, Neck-down and thermally induced defects in high-speed optical fiber drawing, ASME J. Heat Transfer 122 (2000) 351–362.
[22] J.R. Palmer, Temperature and dopant concentration in single-mode 5-μm diameter optical fiber-cooling through the die: implications for Laguerre orders in optical refractive synchronization, in: Proceedings of SPIE, 2000, pp. 381–400.
[23] V.K. Garg, P.K. Maji, Flow through a converging–diverging tube with constant wall enthalpy, Numer. Heat Transfer 12 (1987) 285–305.
[24] K.C. Karki, S.V. Patankar, Pressure based calculation for viscous flows at all speeds in arbitrary configurations, AIAA J. 27 (9) (1989) 1167–1174.
[25] M.C. Melaaen, Calculation of fluid flows with staggered and nonstaggered curvilinear nonorthogonal grids—a comparison, Numer. Heat Transfer Part B 21 (1992) 21–39.
[26] M. Vinokur, Conservation equations of gas dynamics in curvilinear coordinate systems, J. Comput. Phys. 14 (1974) 105–125.
[27] J.W. Fleming, C.R. Kurkjian, Measurement of cation diffusion in silica light guides, J. Am. Ceram. Soc. 68 (9) (1985) C246–C248.
[28] J.T. Krause, W.A. Reed, K.L. Walker, Splice loss of single-mode fiber as related to fusion time, temperature, and index profile alteration, J. Lightwave Technol. 4 (7) (1986) 837–840.
[29] K. Shirsishi, Y. Aizawa, S. Kawakami, Beam expanding fiber using thermal diffusion of the dopant, J. Lightwave Technol. 18 (8) (1990) 1151–1161.
[30] Y.Y. Huang, A. Sarkar, P.C. Schultz, Relationship between composition, density and refractive index for germania silica glasses, J. Non-Cryst. Solids 27 (1978) 29–37.
[31] S. Patankar, Numerical Heat Transfer and Fluid Flow, McGraw-Hill, New York, 1980.